We are IntechOpen, the world's leading publisher of Open Access books
Built by scientists, for scientists

7,200
Open access books available

191,000
International authors and editors

210M
Downloads

Our authors are among the

154
Countries delivered to

TOP 1%
most cited scientists

14%
Contributors from top 500 universities

CLARIVATE ANALYTICS
BOOK CITATION INDEX
INDEXED

WEB OF SCIENCE™

Selection of our books indexed in the Book Citation Index
in Web of Science™ Core Collection (BKCI)

Interested in publishing with us?
Contact book.department@intechopen.com

Numbers displayed above are based on latest data collected.
For more information visit www.intechopen.com

Residual Stress Pattern Prediction in Spray Transfer Multipass Welding by Means of Numerical Simulation

Jon Ander Esnaola, Ibai Ulacia,
Arkaitz Lopez-Jauregi and Done Ugarte

Additional information is available at the end of the chapter

Abstract

One of the main problems of gas metal arc welding (GMAW) process is the generation of residual stresses (RS), which has a direct impact on the mechanical performance of welded components. Nevertheless, RS pattern prediction is complex and requires the simulation of the welding process. Consequently, most of the currently used dimensioning approaches do not consider RS, leading to design oversized structures. This fact is especially relevant in big structures since it generates high material, manufacturing and product transportation costs. Nowadays, there are different numerical methods to predict the RS generated in GMAW process, being Goldak's method one of the most widely used model. However, the use of these methods during the design process is limited, as they require experimentally defining many parameters. Alternatively, in this chapter, a new methodology to define the heat source energy based on the spray welding physics is exposed. The experimental validation of the methodology conducted for a multipass butt weld case shows good agreement in both the temperature pattern (9.16% deviation) and the RS pattern (42 MPa deviation). Finally, the proposed methodology is extended to analyse the influence of the thickness and the number of passes in the RS pattern of thick T-joint welds.

Keywords: multipass welding, analytic procedure, finite element method, equivalent heat source, temperature distribution, residual stresses

1. Introduction

Gas metal arc welding (GMAW, also referred as metal inert gas (MIG)), is one of the most extended welding techniques in metal manufacturing industry [1, 2]. Particularly, multipass

welding in spray transfer mode presents uniform metal transfer to workpiece at high rate, together with high arc stability and low weld spatter. For this reason, spray transfer mode is especially adequate to join thick plate structures [3, 4].

Nevertheless, one of the main drawbacks of welded structures is the generation of residual stresses (RS), which may compromise their mechanical performance. RS are generated due to high thermal cycles in the welding process where non-uniform heating and cooling occur [5, 6]. High thermal gradients generate inhomogeneous thermal expansion constrained by the surrounding material, which presents temperature-dependent mechanical properties. This way, the material at lower temperature suffers lower thermal expansion and presents higher strength. Thus, they also limit the expansion of adjacent areas at higher temperature which, in addition, present lower strength and, consequently, can suffer compressive plastic deformation. Finally, during the cooling down process, the areas yielded at high temperature constrain the elastic springback of not yielded areas generating internal stresses that remain on the welded component. This RS can be tractive or compressive depending on the constraints transmitted from the adjacent areas. As a result, tensile and compressive areas as well as the magnitude of the final RS pattern depend on several factors such as structural dimension, welding sequence, preparation of the weld groove, mechanical restraints or the number of weld passes [7–9]. In general, tensile residual stresses are considered detrimental because they increase the suscepti-bility of the welded joint to fatigue damage, stress-cracking corrosion (SCC), structural buckling and brittle fracture [6, 10, 11].

Figure 1 shows an example of the RS evolution of a determined point (dx, dy) of a plate near the weld seam depending on the thermal history subjected during the welding process of a
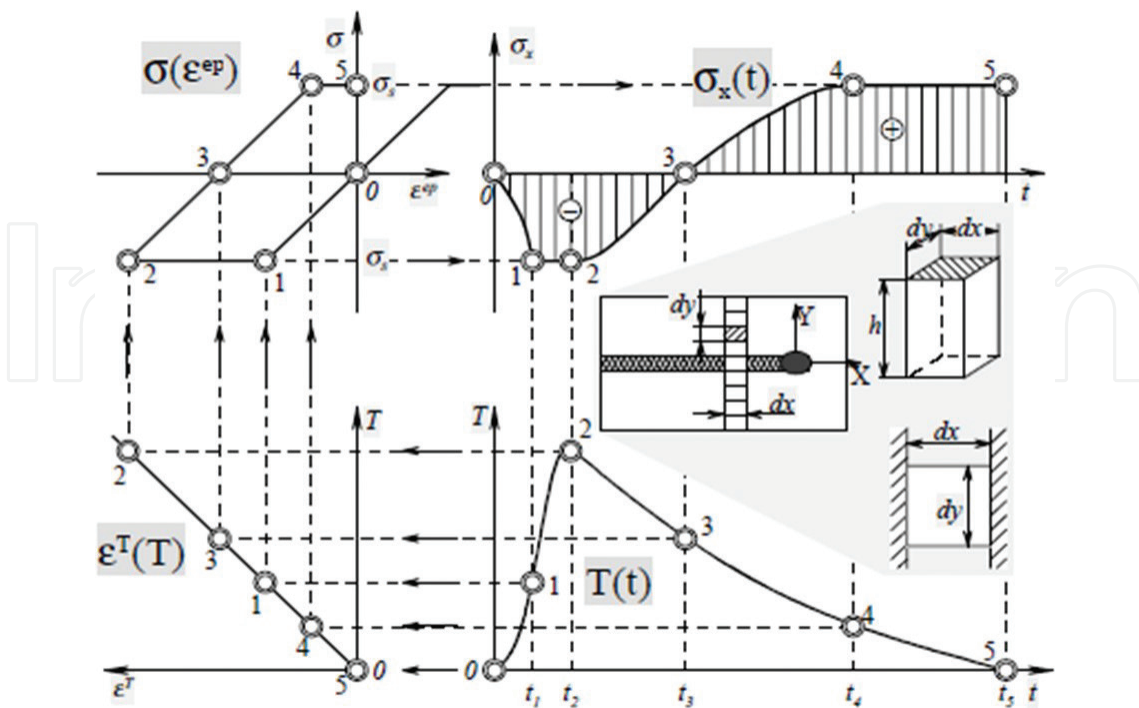

**Figure 1.** Schematic of the RS generation in a generic point nearby the welded seam [12].

butt weld [12]. It can be observed that from instant t_0 to t_2, the material is heated up as the welding torch passes nearby trying to expand. The constraints of the surrounding material limit its expansion in x direction up to ε^T_2, and the initially stress-free material is compressed yielding at σ_1 and suffering elastic-plastic deformation ε^{ep}_2 at high temperature T_2 up to σ_2. Then, during the cooling down process from instant t_2 to instant t_5, the elastic recovery from thermal expansion is limited by the surrounding material. Consequently, tensile stress that yields at σ_4 is generated suffering plastic deformation up to σ_5.

Figure 2 compares the RS pattern variation near the weld toe for a butt weld case depending on the plate size and welding deposition rate. It can be observed that the distribution and magnitude of tractive and compressive stresses completely changes when modifying any of the selected parameters [13].

Due to the complexity of the multiphysics phenomena that take place in the RS generation of welded structures, the estimation of their magnitude and distribution is not straight forward [14, 15]. In addition, nowadays accurate experimental measurement of RS presents some limitations as experimental methods are not fully reliable and imply huge time and economic cost [9, 16, 17]. Consequently, most of the currently used welding dimensioning approaches do not consider RS. Therefore, current welded designs are in general conservative, leading to oversized structures. This fact is especially relevant in big structures since it generates high material, manufacturing and product transportation costs. As a simplified manner to take into account RS, some authors consider the yield stress value as RS magnitude [18–20].

However, nowadays the RS distribution and magnitude can be estimated by means of numerical simulation [14, 21]. As already explained, the RS generation in welded plates is very dependent on the thermal pattern history along the whole component as well as the materials thermomechanical properties. Thus, the procedure used to model the moving heat source during the welding process simulation is determinant in the accuracy of the predicted RS pattern [22].

Different approaches to model the heat source energy can be found in the literature. In the early 1940s, Rosenthal presented an analytic model to consider heat source at a quasi-steady regime, concentrated in a moving point [23]. Although the model could be applied in simple geometries, it was not suitable to be used at plates over certain thickness [2, 6]. At the end of
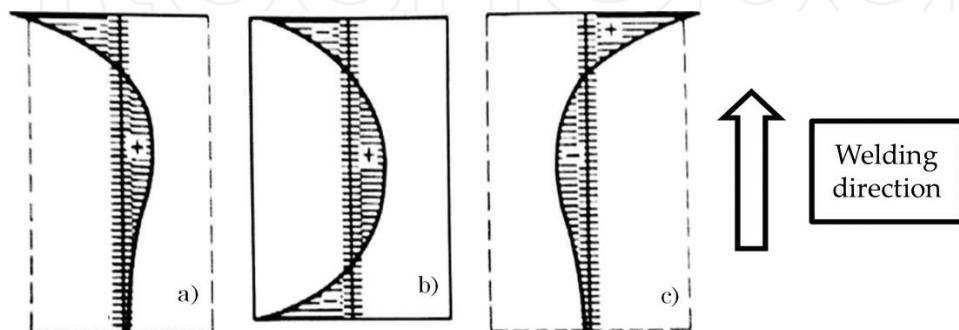

Figure 2. Transversal RS distribution near the weld toe of a butt weld: (a) under high deposition speed in a big plate, (b) high deposition speed in a short plate and (c) low deposition speed in a big plate [13].

1960s, Pavelic et al. [24] proposed a procedure to model as a moving circular heat input area with a Gaussian distribution of the heat intensity. The model considers that all the heat supplies occur through the surface, which also limits its use over certain plate thickness.

In 1984, Goldak et al. presented an alternative heat source model, known as the double ellipsoidal method or Goldak's method, which is one of the most extended methods nowadays [25–30]. This method considers a double ellipsoidal power density distribution (**Figure 3**). This method presents good accuracy even though it requires experimental run trials to measure the weld pool. These measurements should be conducted during or after finishing the welding process, which limits its use as a predictive tool [31]. In addition, the measurement of the weld pool for certain configurations such as T-joints or L-joints is geometrically limited. In 1997, Wahab et al. [32] developed some analytical equations based on experimental measurements to predict the weld pool depending on the applied voltage, current intensity, welding speed and CO_2%. Nevertheless, even these analytical equations enable the use of Goldak's method as a predictive tool, it still presents a lack of precision with reported stress deviations higher than 100 MPa [10].

In 1998, Brickstad et al. [7] proposed a heat source modelling technique where the current and voltage applied in the welding process were used as input parameters. The technique was implemented to simulate a case study of a multipass butt weld of stainless steel pipes by means of a two-dimensional axisymmetric numeric model. The validity of the model was not evaluated against experimental data. In 2007, Barsoum et al. [33] implemented the same technique also in a three-dimensional model to simulate a multipass welding of a tubular joint. The results obtained in the experimental validation showed that even the temperature prediction for a single pass butt weld was accurate, the model presents a lack of precision for multipass cases. In addition, in this method the calculated temperature histories are set into agreement with experimental data measured by thermocouples. If there is no experimental data available, the welding parameters are adjusted to achieve a reasonable molten zone size and distance to the HAZ from the fusion zone boundary [30].

Finally, from 2007 to 2009, Hu et al. [34–36] presented several works were a 3D mathematical model was implemented to represent the physics of the plasma arc and the metal transfer in
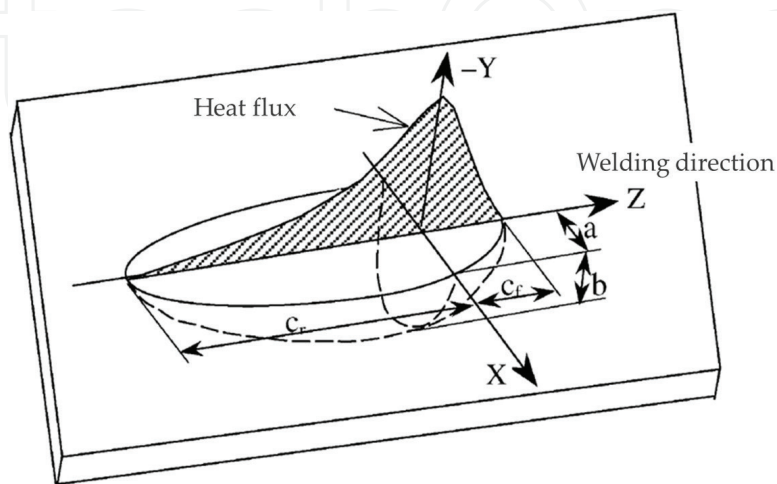
Figure 3. Schematic of the heat source modelization with Goldak's double-ellipsoidal method [25].

order to solve accuracy limitations. This method, besides the computational cost, requires the definition of many parameters such as the arc plasma viscosity, the arc plasma temperature, the surface tension coefficient, etc. The complexity to determine those parameters together with the high computational cost limits the use of this technique.

In general, the presented methods are sometimes imprecise or require defining experimentally many parameters, which limit their use during the design process. As an alternative, in this chapter an analytic procedure to calculate the welding process key parameters is presented. The procedure is based on the welding physics for spray transfer, and the key parameters are analytically estimated. Thus, the procedure feeds the FEM numerical model without the need to conduct experimental process measurements, which enables to be used as a predictive tool. The proposed procedure has been experimentally validated. First, the heat source model has been verified, and then the temperature pattern and the residual stress pattern predicted by the FEM model have been compared against experimental measurements. The main contribution of the presented procedure is that it provides an agreement between the accuracy of the model in the residual stress estimation, the computational cost and the model definition effort. In addition, the new procedure does not require any preliminary experimental welding test data, which make it suitable to be used in the design process.

Finally, the proposed procedure is extended to a T-joint configuration with 70% penetration in a thickness range from 20 to 60 mm to determine the influence of the thickness and number of passes in the RS pattern.

2. New methodology to predict RS

The proposed methodology to predict RS consists of two steps. First, the process key parameters, which are the heat source and the welding speed, are defined. For that purpose, an analytic procedure to determine the heat source and welding speed that ensure proper spray transfer welding is developed. Then, an uncoupled thermomechanical FEM model is used to simulate the welding process. This numerical model is fed from the previously defined process key parameters.

2.1. Determination of process key parameters

The multipass spray transfer welding numerical model requires the determination of the heat source energy and the welding speed as input data. Both parameters are estimated based on the welding torch configuration and the cross section to weld.

Figure 4 shows the detail of the configuration of the welding torch, where L_{arc} is the arc length, L_{CTW} is the contact to work distance and L_{SO} is the wire extension or electrical stick-out length.

2.1.1. Heat source energy

The heat source energy is the thermal energy provided to the weld bead along the welding process. This parameter is calculated considering the efficiency in the transformation of the
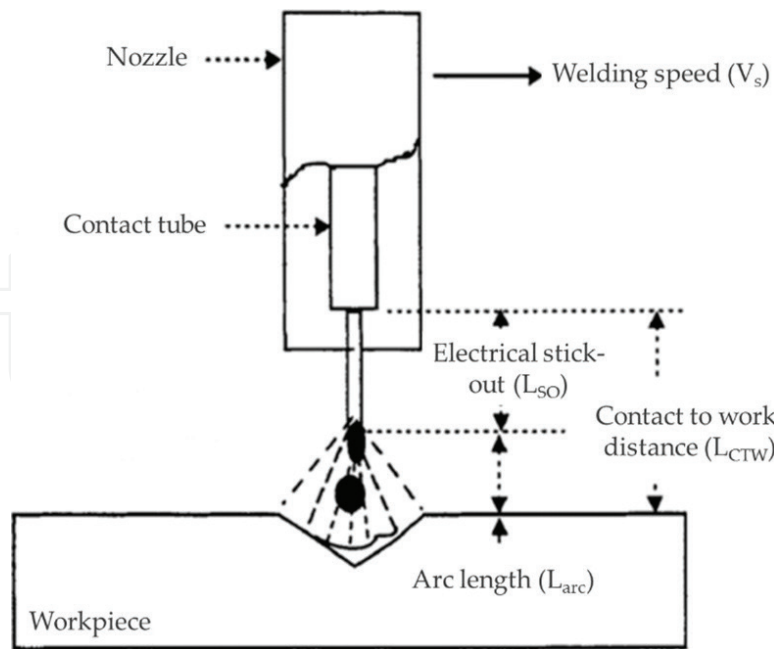
Figure 4. Schematic of the welding torch configuration (adapted from [1]).

consumed electric power into heat power. This energy lose is caused by the wire resistance, heat losses to the surrounding, the energy consumed in the gas or flux heating, etc. Thus, efficiency can vary between 0.66 and 0.85 depending on the used facility [1]. Therefore, the supplied heat power can be determined with Eq. (1):

$$P_{TH} = \eta \cdot I \cdot V_{Tot} \tag{1}$$

where P_{TH} is the supplied thermal power, η is the heat transformation efficiency, I is the current intensity and V_{Tot} is the total voltage.

In order to ensure proper spray transfer, the transition welding intensity between globular and spray transfer modes is determined first. This parameter is dependent on the used shielding gas and filler wire diameter. Thus, using current intensity values higher than the transition current intensity limit value provides proper spray transfer. **Figure 5** represents the correlations proposed by Norrish [37] to determine the globular-to-spray mode transition current depending on the shielding gas for a wire diameter range between 0.8 and 1.6 mm.

The total voltage drop V_{Tot} is approximately the addition of the voltage drop in the electric stick-out length V_{so} and the voltage drop across the arc V_{arc} (2) [1].

$$V_{Tot} = V_{arc} + V_{so} \tag{2}$$

The arc voltage drop can be obtained with Eq. (3):

$$V_{arc} = I \cdot R_{arc} + a_0 + a_1 \cdot L_{arc} \tag{3}$$
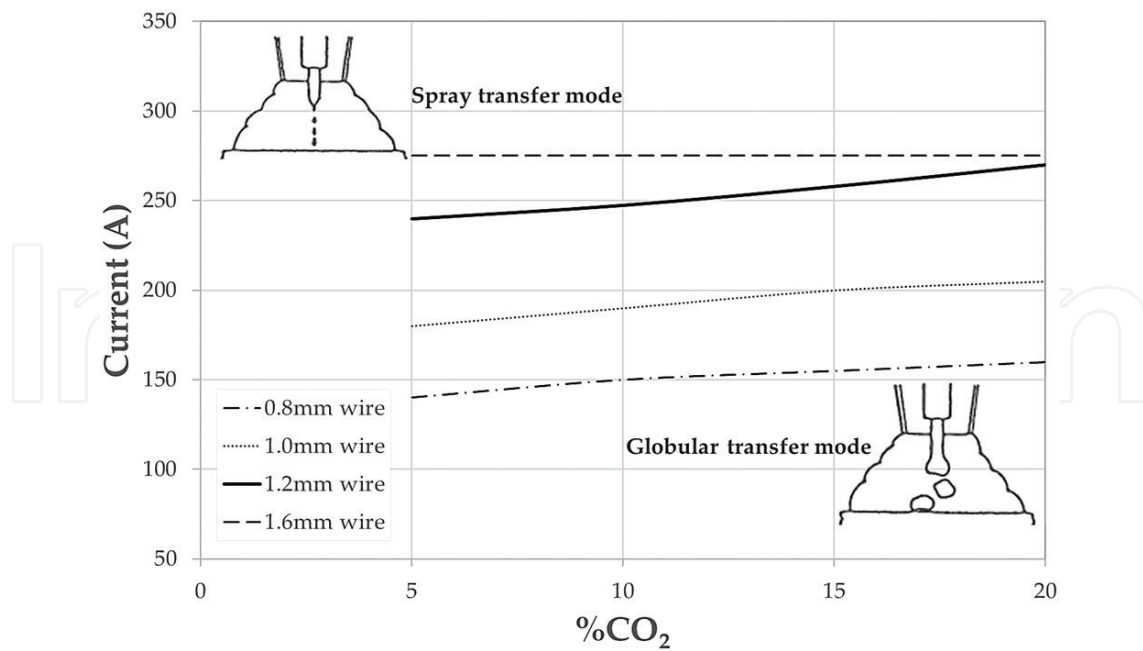
Figure 5. Globular mode to spray mode transition current depending on the use of shielding gas for wire diameter range between 0.8 and 1.6 mm (adapted from [37]).

where R_{arc} is the arc electric resistance, a_0 is the anode/cathode voltage drop and a_1 is the arc potential gradient. The minimum L_{arc} to ensure spray transfer has to be higher than 4.5 mm according to Lesnewich [48].

The voltage drop across the electrode is calculated with Eq. (4):

$$V_{so} = \rho_s \frac{L_{so}}{A_{so}} I \qquad (4)$$

where ρ_s is the resistivity of the stick-out material and A_{so} is the cross-section area of the wire.

The stick-out length L_{so} (**Figure 4**) is determined with Eq. (5):

$$L_{so} = L_{CTW} - L_{arc} \qquad (5)$$

2.1.2. Welding speed

The welding speed is the velocity the welding torch advances along the welding bead. It is assumed that GMAW process fulfils the mass conservation law. Thus, wire feed speed and welding speed can be determined by Eq. (6):

$$A_{so} \cdot v_W = A_s \cdot v_s \rightarrow v_s = \frac{A_{so} \cdot v_W}{A_s} \qquad (6)$$

where v_W is the wire feed speed, A_s is the weld pass cross section and v_s is the welding speed.

There are two approaches to model the wire feed rate for constant voltage welding used in GMAW, as suggested by Palani et al. (2007) [39]. The first approach consists in fitting the

equation relating welding current and wire feed rate with experimental data. The second approach consists in using the results of the experiments to determine the constants of proportionality for the arc heating and the electrical resistance heating.

In the methodology presented in this chapter, the second approach is used. Thus, the wire feed speed is calculated with Eq. (7) [37]:

$$v_W = \alpha \cdot I + \frac{\beta \cdot L_{so} \cdot I^2}{A_{so}} \tag{7}$$

where α and β are constants dependent on the used wire properties.

Moreover, considering different values of the constants (α and β) from several studies for solid plain carbon steel wire analysed from literature (Norrish 1992 [37], Murray 2002 [40], Modenesi 2007 [41], Palani 2006 [42], Palani 2007 [39]), it is observed that their difference is negligible (**Figure 6**). Therefore, in the present work, it is decided to consider the values defined in [37], $\alpha \approx 0.3$ mmA-1 s-1 and $\beta \approx 5 \cdot 10^{-5}$ A-2 s-1 for a 1.2 mm plain carbon steel wire.

2.2. Uncoupled thermomechanical FEM modelling procedure

Welding is a thermometallurgical process where the thermal field directly affects in the mechanical domain response, but the effect of the mechanical field on the thermal domain can be considered negligible as dimensional changes in the welding process are not representative and generated deformation energy is insignificant compared to the thermal energy from the welding arc [43]. Thus, the welding process can be modelled with an uncoupled
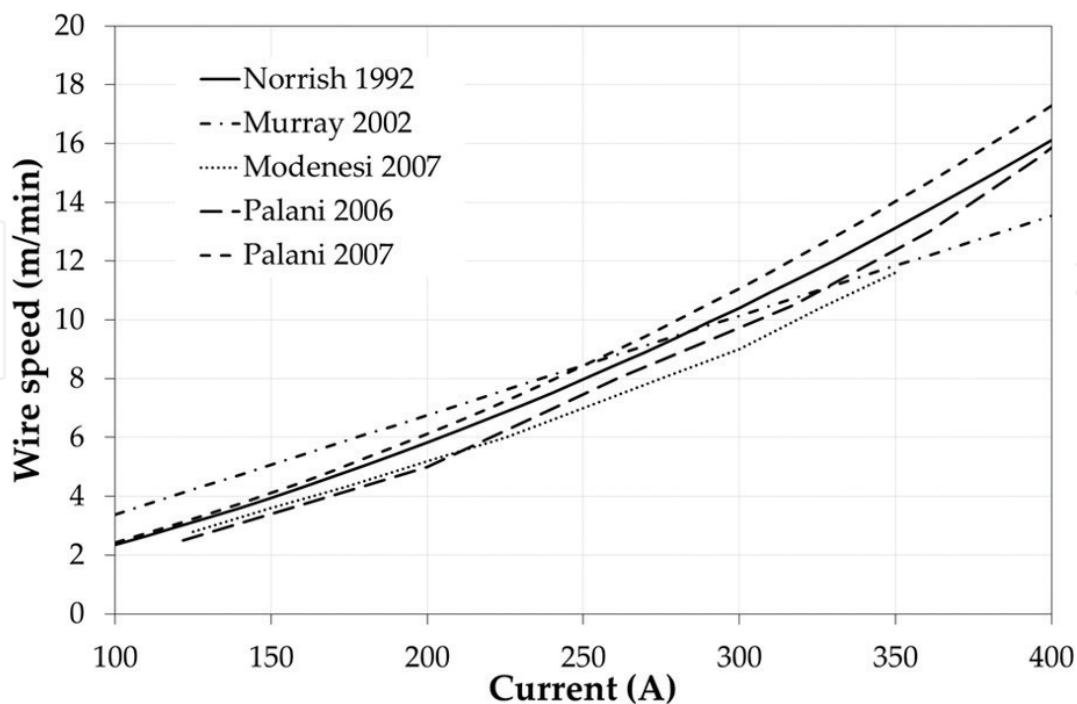
Figure 6. Comparison of different approaches to determine wire speed based on welding intensity for carbon steel filler (adapted from [37, 39–42]).

thermomechanical approach where the thermal domain is solved first. Then, the mechanical field is solved fed by the previously calculated thermal pattern history. Consequently, computational cost can be significantly reduced. Both equation systems are solved by using the implicit direct integration method.

Even though both models are solved separately, they share same geometric model where just the element type and restrictions differ.
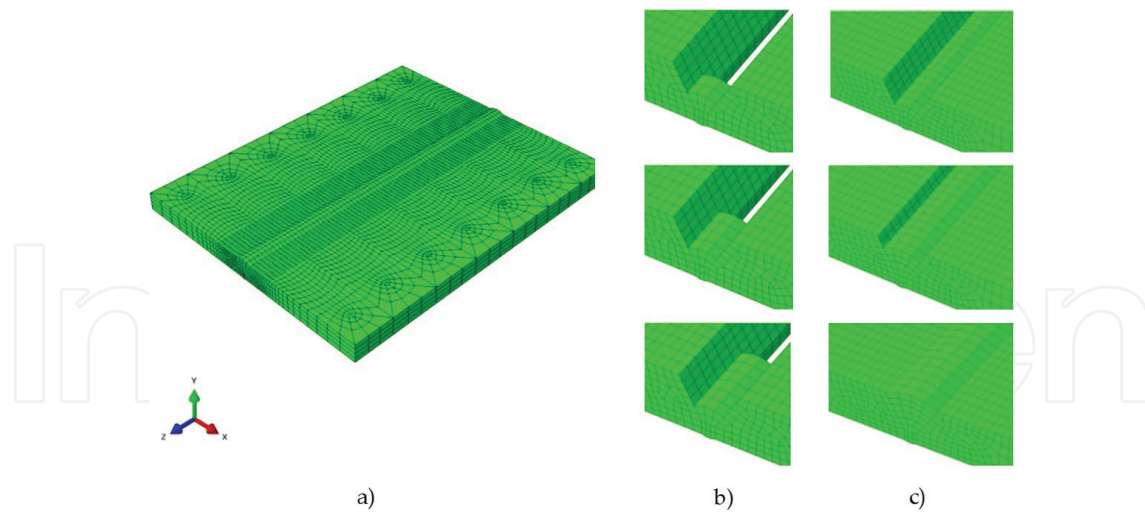
2.2.1. Geometric model

The geometric model has to include the geometry of each welding pass based on the calculated cross section for each pass. According to Teng et al. [44], the flank angle does not have significant effect in the residual stress value. For this reason, considering the real geometry of the plates to weld, a flank angle of 30° has been selected to define the bead radius (see **Figure 7**). The arcs for the bead in the rest of the passes are defined concentric with respect to the last pass by keeping the value of the initially calculated cross section for each pass.

The model is meshed by using full integration continuum hexahedral elements (recommended) where the proper formulation is selected, respectively, to solve the thermal domain and the mechanical domain (**Figure 8a**). The addition of filler material through each pass is modelled by using the kill/rebirth method [13, 22, 26] (**Figure 8b** and **c**). In this method, all the weld bead elements are initially inactive and, consequently, eliminated from the equation system. Then, elements are activated in function of the welding speed (v_s), simulating the welding torch pass. In order to ensure sufficient resolution in the transient temperature evolution, a temporal discretization of one second is specified. Symmetry is not considered as an asymmetric clamping condition where just one plate end is fixed to avoid during the validation the influence of the boundary restrictions in the predicted RS pattern (in accordance with the used experimental set-up).
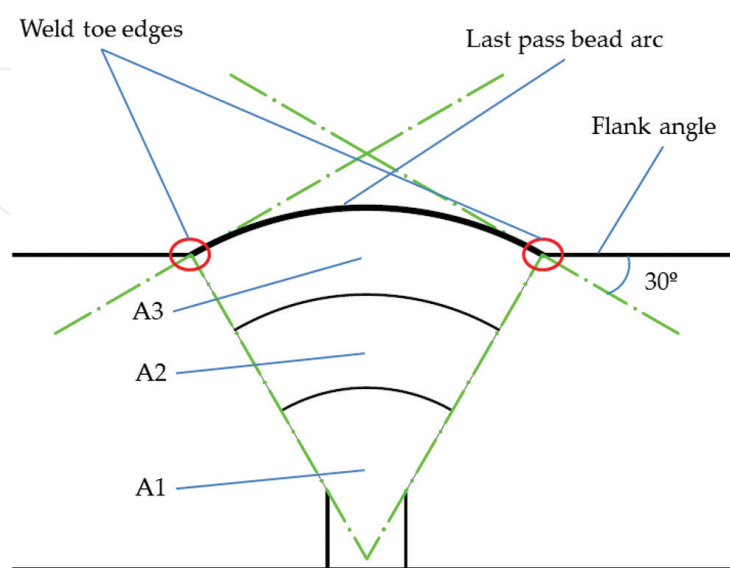
Figure 7. Schematic of the procedure to calculate the weld bead geometry for each pass for a three-pass weld case.

a)   b)   c)

Figure 8. (a) Example of a full geometric model of a multipass butt weld, (b) principle of the addition the weld bead and (c) multipass welding modelling of a three-pass weld case.

2.2.2. Material

Temperature-dependent thermal and thermomechanical properties of both plate material and filler material have to be defined to feed de thermal model and mechanical model, respectively:

- **Modelization of the thermal field:** Density, latent heat, thermal conductivity as well as specific heat are required.

- **Modelization of mechanical field:** Density, Young modulus, Poisson ration, thermal expansion coefficient as well flow stress curves are required.

Regarding phase transformation effects, the aim of the present modelling methodology is to reach to an agreement between the model simplicity and accuracy level. Therefore, even effect of phase transformation in the temperature-dependent properties such as density, thermal expansion or specific heat is considered, the mechanism of phase transformation is not included in the model. Some studies in the literature as the work presented by Payares-Asprino et al. in 2008 [45] have shown that this phase transformation could be significant for low temperature transformation (LTT) filler materials. However, in the present study, a conventional filler material is used, where the expansion that material suffers by martensitic transformation is relatively small and occurs at relatively high transformation temperature range. Consequently, its effect in the generated residual stresses and distortions is not significant [46].

2.2.3. Loads and boundary conditions

- **Modelization of the thermal field:** Based on the previously exposed analytic procedure, heat source is implemented as uniform body heat flux over the elements activated at the rebirth speed corresponding to the welding speed. Natural convection of the free surfaces as well as radiation should be considered.

- **Modelization of mechanical field**: Clamping restraints have to be considered as boundary conditions. In addition, temperature pattern is fed from the previously calculated thermal model considering the rebirth speed corresponding to the welding speed. Once the welding process and cooling down process are completed, clamping restrains are deactivated to obtain final RS pattern.

3. Methodology implementation and experimental validation

The proposed procedure is implemented and validated for a case study of three-pass spray transfer butt weld of 10 mm thick and 200 mm length of two S275JR steel plates (see **Figure 9**). The used filler material is a 1.2 mm wire diameter PRAXAIR M-86 according to the AWS/ASME SFA 5.18 ER70S-6 standard. Stargon 82, with 8% of CO_2, is used as shielding gas.

3.1. Numerical procedure

The heat transfer model as well as the mechanical model used for the simulation of the welding process of the selected case study is implemented in the simulation software ABAQUS™.

3.1.1. Geometric model

A critical activation length per second of 6.12 mm is calculated to ensure temporal discretisation of 1 s for the third pass, which is conducted with the lower welding speed. Consequently, a 5 mm length discretization size, which ensures a temporal discretization <1 s for the three passes, is selected for the presented work. Furthermore, it allows fitting exactly with 40 discretization volumes the 200 mm length of each pass.

3.1.2. Material

Table 1 shows the standard mechanical properties of S275JR structural steel used for the welded plated and the PRAXAIR M-86 filler material at room temperature. As it can be observed, both materials show similar ultimate strain and ultimate strength, but the yield stress of the filler material is 45% higher.
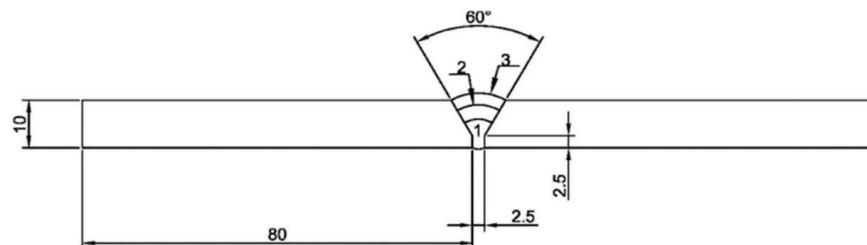
Figure 9. Welding configuration of the analysed case study.

	σ_y (MPa)	σ_u (MPa)	A (%)	E (GPa)
S275JR	275	430–580	23	190–210
Filler M-86	>400	>480	>22	200

Table 1. Standard mechanical properties of S275JR structural steel [47] and PRAXAIR M-86 filler material [48, 49].

Temperature-dependent flow stress curves at a quasi-static strain rate for the filler material are estimated based on S275JR data and considering a 45% higher temperature-dependent yield stress value. The rest of thermomechanical properties as well as thermal properties are considered the same as the base material. This simplification is considered acceptable according to the next statements:

- Considering same thermal properties as will have minor influence in the estimated temperature distribution and thermal expansion as both steels present similar, conductivity, specific heat, latent heat and thermal expansion.

- Same temperature-dependent density and elastic modulus can be considered for both the base material and filler material, as low variations in the content of alloying elements of structural steels have insignificant influence in these parameters [49].

- The temperature-dependent yield stress of the filler material is assumed to be 45% higher than the base material. As the plastic deformation level found in the welding process is low, near the yield stress values, considering the same temperature-dependent tangent modulus will not have significant effect in the predicted RS pattern.

- The cross section of the weld bead is small in comparison with both plates' cross section. For this reason, considering same thermal expansion value as for the base material will generate an insignificant deviation in comparison with the total thermal expansion. Consequently, it is considered that possible error gene rated from the previous assumptions in the computed transversal residual stress will be negligible.

3.1.3. Thermal properties

Figure 10a shows the utilised temperature-dependent density, thermal conductivity and specific heat data for both filler and plate materials. **Table 2** shows the considered latent heat and solidus-liquidus transition temperature.

3.1.4. Thermomechanical properties

Figure 10b–d shows the temperature-dependent mechanical properties for both the base material and filler material.

3.2. Loads and boundary conditions

3.2.1. Heat transfer model

Heat source and welding speed for the specified case study are obtained with the new methodology exposed in Section 2. First, in order to determine the efficiency of the used welding
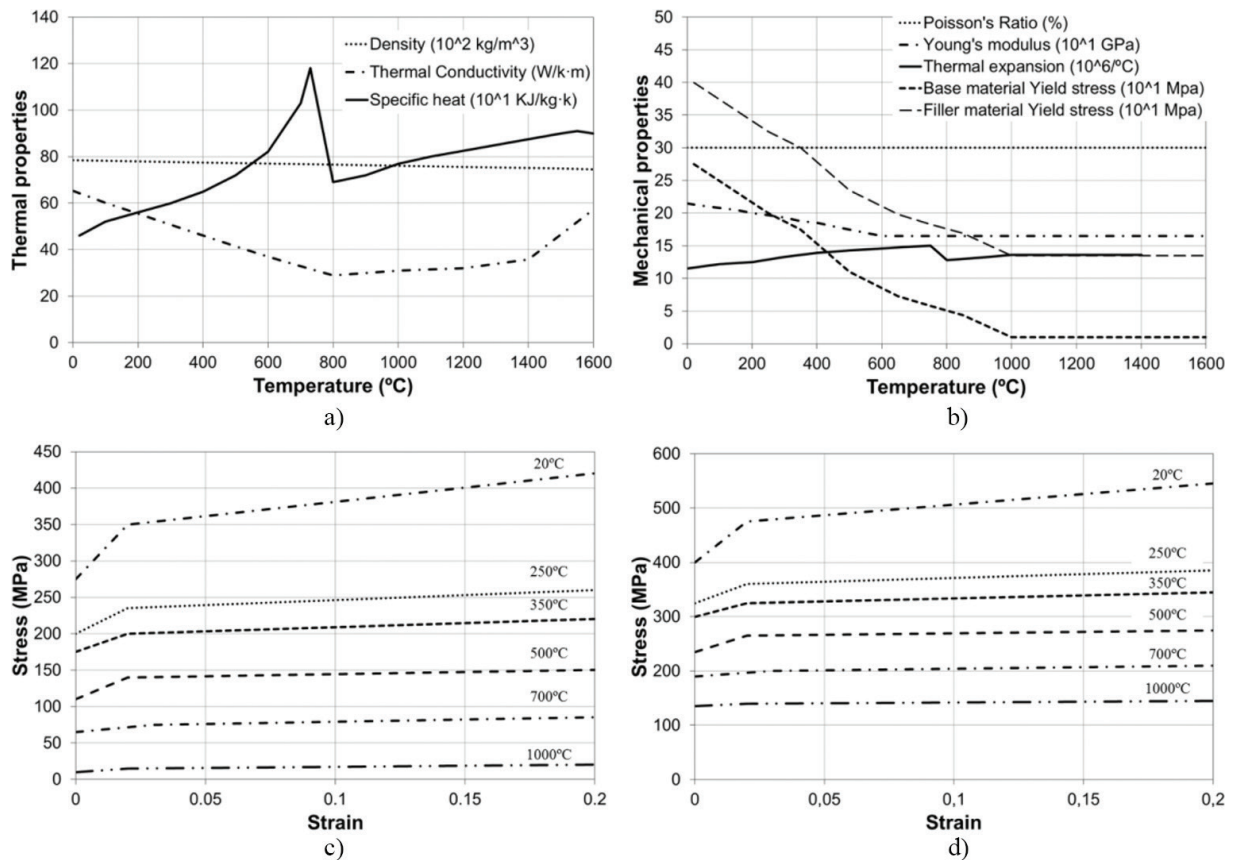
Figure 10. Temperature-dependant material properties. (a) Specific heat taken from [50], thermal conductivity taken from [22, 51] and density taken from [46]; (b) Young's modulus and thermal expansion taken from [52] and yield stress taken from [53, 54]; (c) plastic properties for the base material [22]; and (d) estimated plastic properties for the wire material.

Latent heat (kJ/kg)	Solidus temperature (°C)	Liquidus temperature (°C)
247	1500	1550

Table 2. Latent heat of fusion [36].

facility, simulations for an efficiency range between 0.6 and 1 are conducted. **Table 3** shows the heat source power for each pass calculated with the following parameters:

- **Transition welding intensity for spray transfer:** The use of a 1.2 mm wire diameter and Stargon 82 as shielding gas, which contains 8% CO_2 [55], determines a minimum welding intensity of 245A to ensure proper spray transfer model. Therefore, for the present case study, an intensity value of 275 A, 12% higher than the transition limit, is used.

- **Wire properties:** The resistivity value of the used wire is R_{arc} 0.0237 Ω [3]. The parameters a_0 and a_1 are set as 6.3 V and 1.55 V/mm respectively based on [4].

- **Welding torch configuration:** A 9 mm L_{arc} (> L_{arc_min} of 4.5 mm [38]) and a 30 mm L_{CTW} are defined. For carbon steels [1], a 0.2821 $\frac{\Omega}{m}$ resistivity of the stick-out material is set.

Efficiency (%)	Power (W)		
	First pass	Second pass	Third pass
1	7755	7755	7755
0.9	6980	6980	6980
0.85	6592	6592	6592
0.8	6204	6204	6204
0.75	5816	5816	5816
0.7	5429	5429	5429
0.6	4653	4653	4653

Table 3. Values of the heat power for different efficiencies.

Welding speed to be implemented as element rebirth rate has been calculated for each pass by using the parabolic model constants $\alpha \approx 0.3$ mmA-1 s-1 and $\beta \approx 5 \cdot 10^{-5}$ A-2 s-1 for a 1.2 mm plain carbon steel wire [37]. Thus, the calculated welding speeds for each pass of the case study in the present work are 545.33, 482.53 and 367.79 mm/min.

Finally, a natural convection boundary condition has been assumed in all surfaces exposed to air of both plates and the rebirthed weld bead elements.

3.2.2. Uncoupled thermomechanical model

Temperature pattern at every iteration is fed from the previously run heat transfer simulation results. As a boundary condition, one of the plate end surfaces is assumed to be fully constrained.

3.3. Experimental procedure

Figure 11 shows the CNC milling machined adapted with a Praxair Phoenix 421 welding machine in order to perform the welding process automatically. This enables to control all the

a)   b)
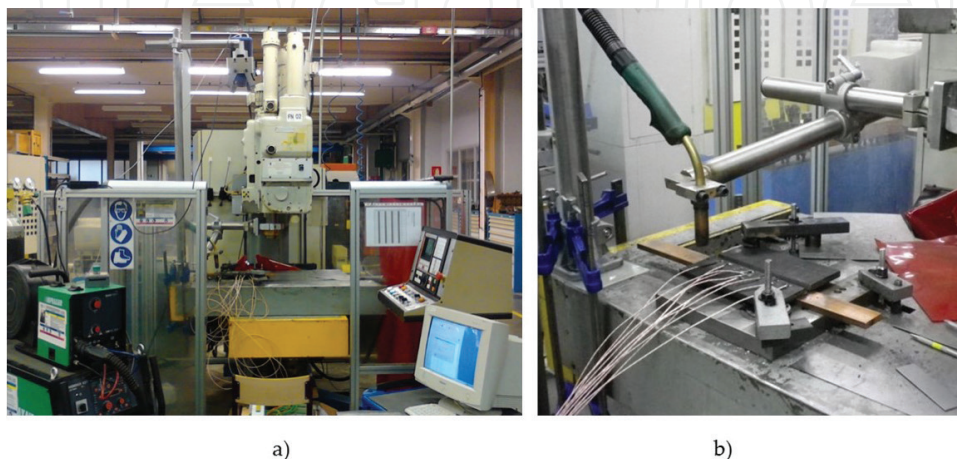
Figure 11. a) Set-up to automatically perform the welding process and b) Detail of the welding configuration.

process parameters such as the arc voltage, the arc length, the contact to workpiece length, the wire feed speed and the welding speed along the whole process. In addition, current intensity and voltage during the whole process are monitored by means of a TPS2024B Tektronix oscilloscope, a PR HAMEG HZ115 voltmeter and a LEM PR 200 ammeter.

In order to conduct the validation of the proposed modelling methodology, temperature patter evolution during the welding process and the RS pattern of the welded samples are also measured.

3.4. Welding procedure

S275JR plates of 10 mm thick and 200 mm length are butt welded in three passes (**Figure 9**) with a 1.2 mm diameter PRAXAIR M-86 filler material. Stargon 82, with 8% of CO_2 [54], is used as shielding gas.

Welding process parameters for each pass are previously determined with the proposed analytical procedure for spray transfer mode (**Table 4**).

3.4.1. Temperature pattern measurement

Temperature pattern history is acquired along the whole process to determine the welding facility's efficiency and to validate the numerically obtained temperature pattern. For this purpose two methods are used in parallel: (i) 10 N-type thermocouples (up to 1200°C) are positions parallel and perpendicular to the weld bead (**Figure 12a**) and (ii) a Titanium DC01 9 U-E thermographic camera to record the surface temperature pattern evolution.

To ensure proper temperature pattern measurement with the thermographic camera, plates are painted with a black colour high temperature-resistant paint in which temperature-dependent emissivity is already determined [56]. However, for better accuracy, the temperature acquisition data of the thermocouples is used to calibrate the acquired temperature pattern.

3.4.2. Residual stress measurement

In order to validate the numerically obtained RS pattern and, consequently, the proposed modelling methodology, RS measurements are conducted by using the hole-drilling method.

To conduct the measurements, Vishay EA-06-062RE-120 rosette-type gauges are placed parallel to the welding bead, at a 52.5 mm distance from the weld toe at both sides of the weld bead as shown in **Figure 12**b. Then, hole-drilling tests are carried out in a CNC milling machine according to ASTM E837 standard.

| Pass	V (V)	I (A)	Vw (m/min)	P (W)	Larc (mm)	Lctw (mm)	Vs (mm/min)
1	28.2	275	9.2	7755	9	30	545.33
2	28.2	275	9.2	7755	9	30	482.83
3	28.2	275	9.2	7755	9	30	367.796

Table 4. Welding process parameters.
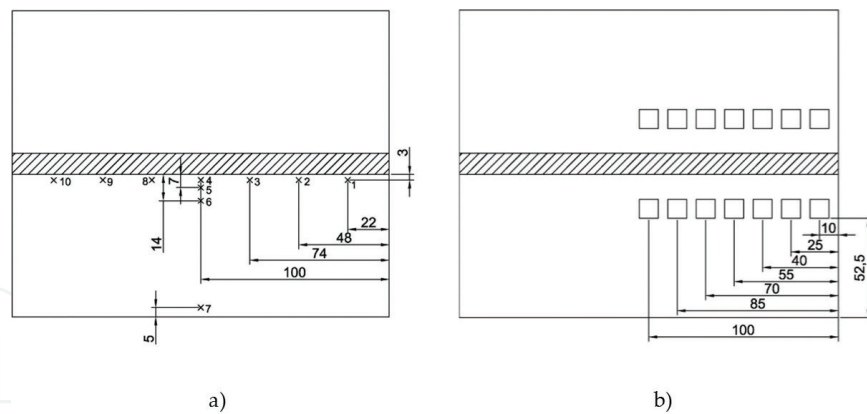
Figure 12. Position of the thermocouples (a) and (b) position of the hole-drilling gauges in the butt weld.

3.5. Results and discussion

In this section, theoretical results and experimental results are compared in order to validate the proposed modelling methodology. For that purpose, first the temperature pattern prediction, which determines the material's thermal expansion, is compared. Then, RS pattern generated by the thermal expansion is validated.

3.6. Temperature pattern validation

Figure 13 shows the comparison of the experimental temperature evolution along the three passes and the theoretically estimated values for an efficiency value of 1. It can be observed that both curves present same process dynamic, where the temperature peaks when the welding torch is near to the reference thermocouple can be clearly identified, followed by a progressive cooling down related to the heat evacuation. In addition, it can be observed that as the cross section of each pass increases, the heat supply for each pass raises and, consequently,
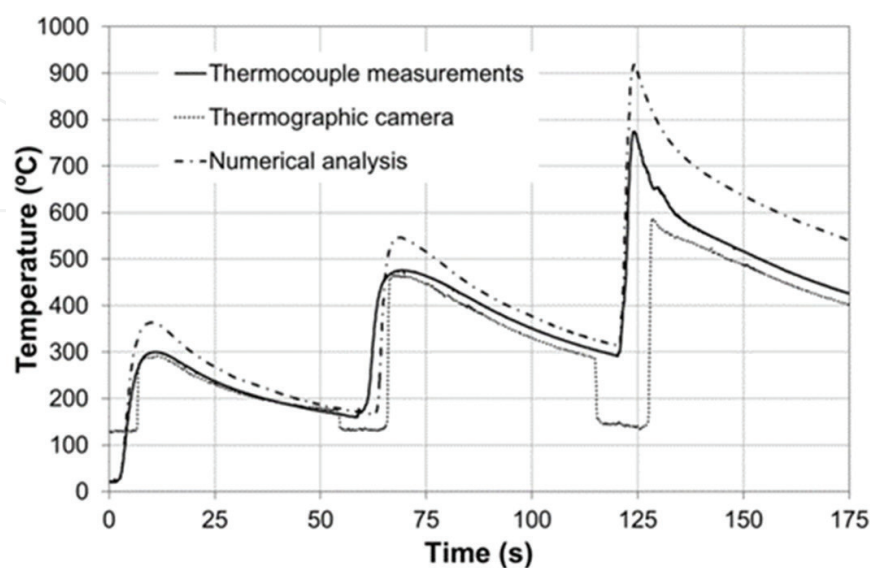
Figure 13. Calculated and measured thermal cycles for thermocouple 1 with an efficiency factor of 1.

the peak temperature value for each pass also increases. From a quantitative point of view, as expected, a theoretical efficiency value of 1 provides higher temperature values than experimentally acquired curves as no power losses are considered.

For this reason, the efficiency of the used welding facility is determined comparing the temperature deviation of all thermocouples at each pass for the simulations conducted in an efficiency range between 0.6 and 1 (**Table 5**). The results show that the highest accuracy is obtained for an efficiency value of 0.8 with an average deviation of 9.16%. Therefore, it is assumed that the efficiency of the facility is 0.8, which is in accordance with the efficiency reference values found in the literature (0.66–0.85) [1].

Figure 14 shows the comparison of the theoretical and experimental temperature evolution for thermocouple 1 for an efficiency of 0.8. An uncertainty attributed to a +/−0.5 mm thermocouple positioning error has been considered in the temperature validation. It can be observed that the temperature evolution present presents a positive quantitative correspondence along the three passes.

In addition, **Figure 15** shows the comparison between the experimental temperature pattern acquired with the thermographic camera and the numerically predicted pattern at the end of each pass for an efficiency value of 0.8. Both temperature patterns show good correspondence in the shape of temperature contours from the high temperature zone over 700°C down to the lower temperature areas at 300°C (limit of the filter use in the thermographic camera).

Considering the low deviation (9.16%) in the temperature evolution prediction together with the positive correspondence found in the temperature pattern contours at each pass, it is concluded that the numerical procedure to predict temperature pattern evolution of multipass spray transfer welding is valid.

3.7. Residual stress validation

Once the performance of the proposed methodology in the thermal field prediction is validated, the RS field is verified to conclude with the model validation.

Efficiency	Error (%)			
	First pass	Second pass	Third pass	Average
1	21.94	20.02	21.77	21.24
0.9	12.8	10.46	16.7	13.33
0.85	8.47	5.82	16.68	10.32
0.8	3.9	5.31	18.26	9.16
0.75	3.45	6.57	19.82	9.95
0.7	6.61	9.97	21.44	12.67
0.6	17.44	20.24	31.17	22.95

Table 5. Calculated error for the peak temperatures at each pass for an efficiency range of 0.6–1.
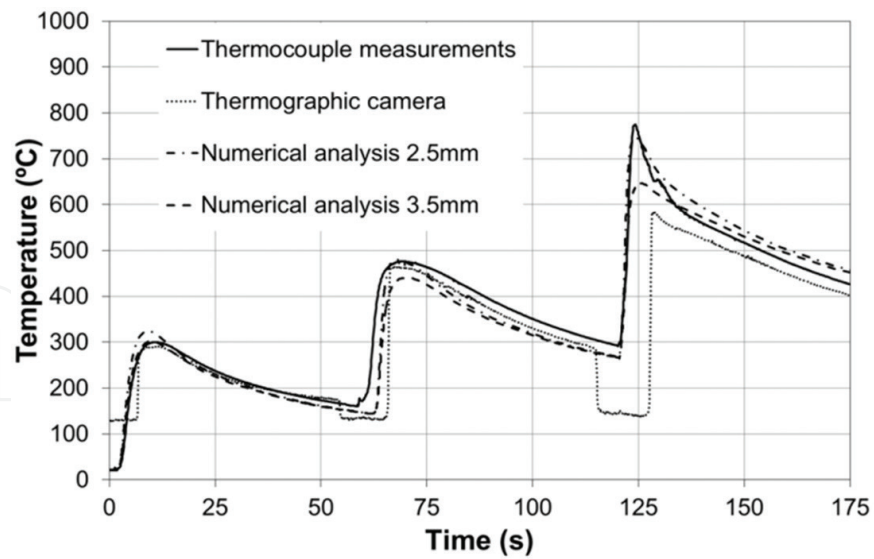
Figure 14. Comparative of experimental versus FEM thermal results for a butt weld with an efficiency factor of 0.8.
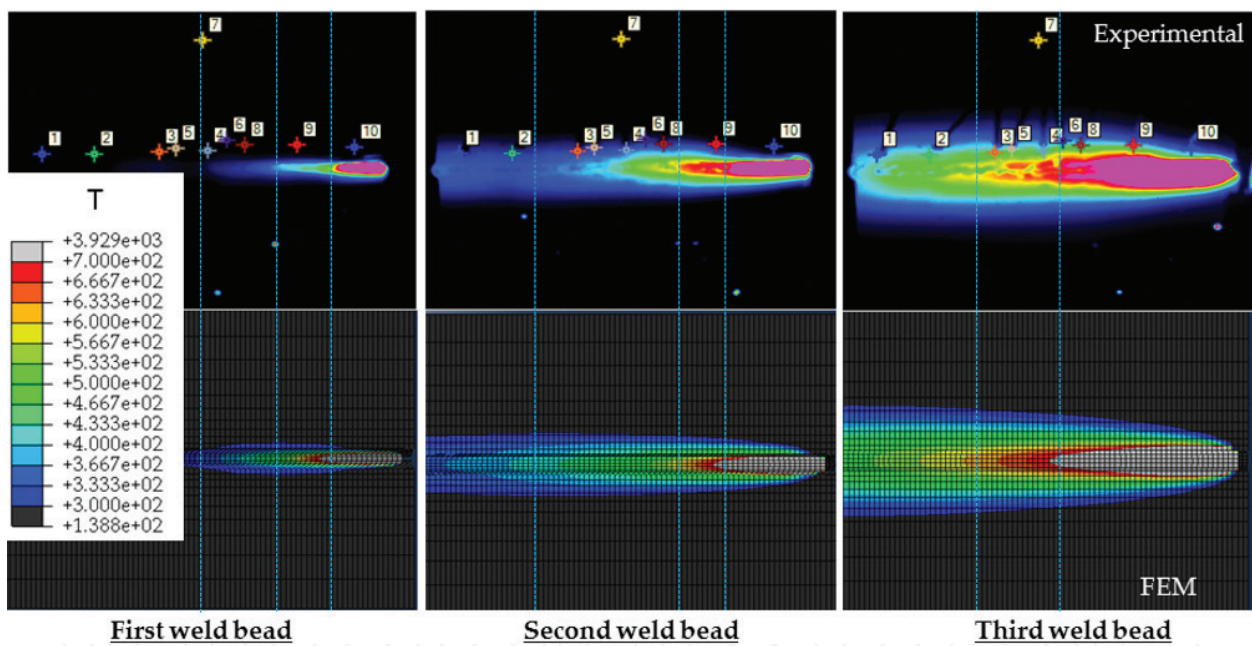

Figure 15. Comparative of experimental versus FEM thermal pattern for a butt weld with an efficiency factor of 0.8 (the points in the upper images are the position of the thermocouples).

Figure 16 shows transverse residual stresses pattern obtained with the FEM uncoupled thermomechanical simulation. A high stress concentration in the clamping area where 6 degrees of freedom are fixed is observed (in accordance with the experimental set-up). However, the stress concentration located in the clamping is far enough from the area of interest, and they do not have any effect in the residual stress validation process. Analysing the area of interest, it is observed that even the stress concentration in the clamping area does not affect the area of interest near the weld bead, the asymmetry in the boundary restriction generates a mild asymmetric
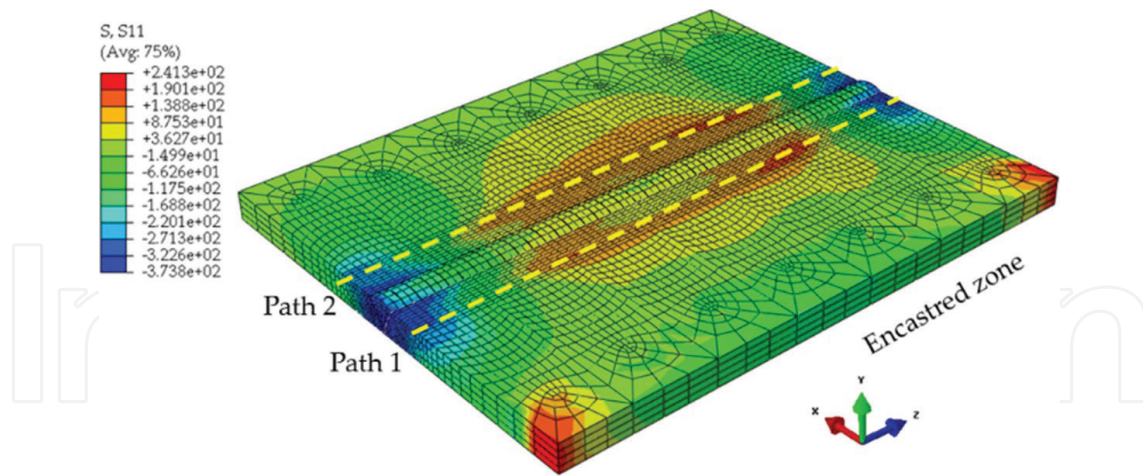
**Figure 16.** Transversal residual stresses pattern for a butt weld.

stress pattern at both sides of the weld seam. Consequently, stress paths at both sides, path 1 and path 2 located in the maximum stress are at each side, are considered for validation purpose.

Figure 17 shows hole-drilling measurements of the transversal residual stress along half of the length (0–100 mm) for both, path 1 and path 2. The results show three differentiated zones: (i) compression zone (0–30 mm), (ii) transition zone (30–60 mm) and (iii) tensile zone (60–100 mm). Additional measurements are conducted in the full length (at 160 mm and 175 mm) to ensure that the RS path shows quasi-symmetric behaviour.

High scatter among the measurement repetitions, inherent to the measuring technique, is observed, which is in accordance with stress deviations up to ±50 MPa reported by some authors [57]. Therefore, average hole-drilling results at each position are considered for both paths to perform the RS validation. **Figure 18a** and **b** shows the comparison between the average hole-drilling results with their standard deviation and simulation results for path 1
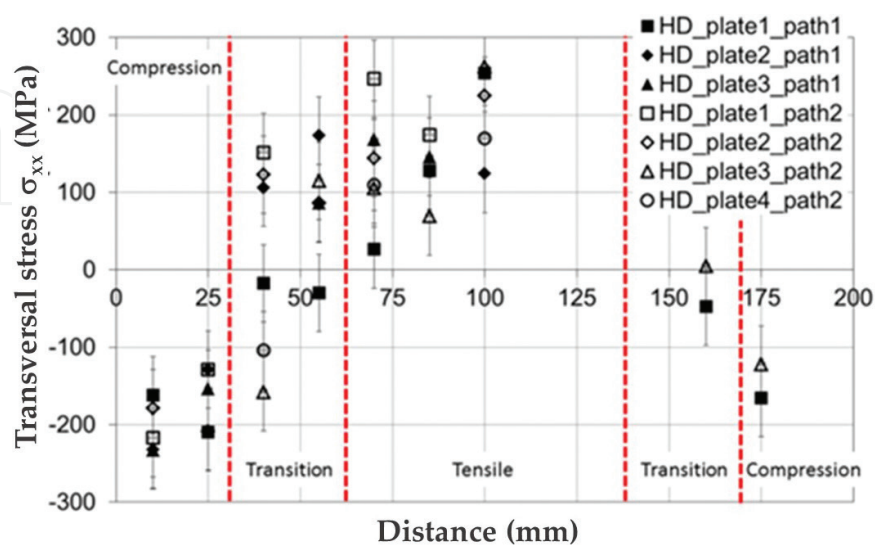
Figure 17. Results of hole-drilling measurements for different plates and for both paths.
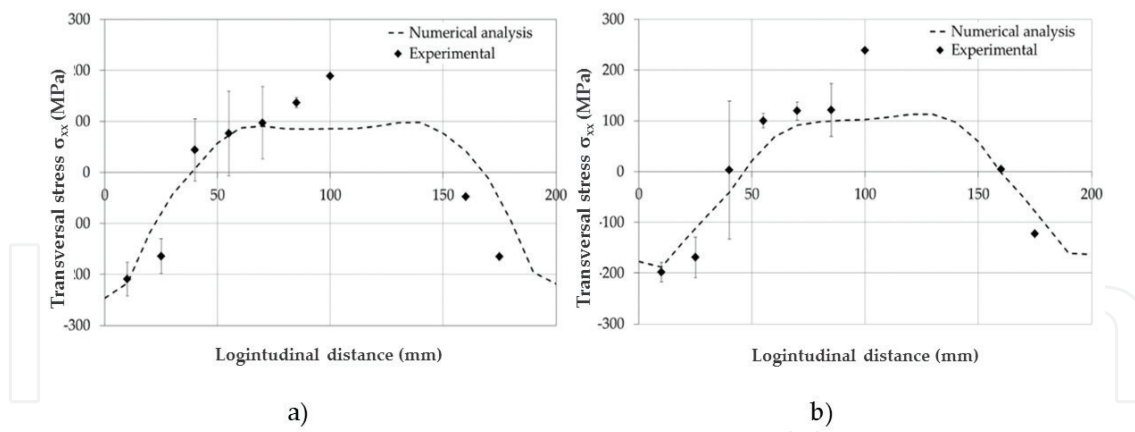
Figure 18. Comparison of the FEM and experimental results for the results of hole.

and path 2, respectively. A positive correspondence is observed between the averaged measurements and the numerical results for both paths where the three zones, compression zone, transition zone and tensile zone, show similar trends. Considering both paths, an average error of 34 MPa, 35 MPa and 57 MPa for each zone, respectively, is calculated with an average total error of 42 MPa. As observed, numerically predicted residual stress values are mostly inside the measurement scatter band (±50 MPa [57]). Thus, it can be concluded that, considering the inherent error of the RS measuring technique, the proposed methodology to predict RS pattern can be considered valid with an average error of 42 MPa.

4. Theoretical analysis of RS pattern on thick T-joint samples

T-joint welding configurations are one of the most widely used in a wide range of structural applications. Particularly, when building large structures, T-joint of thick plates requires high amount of weld passes, and consequently, the RS pattern varies considerably depending on the plate thickness and the number passes, hence affecting to mechanical performance such as fatigue endurance.

Nowadays, most approaches to dimension-welded structures do not consider RS real value due to the difficulty of estimating them; hence, they tend to be conservative. However, recent works [gure erreferentziak] have demonstrated that considering RS, the error for example in fatigue life prediction can be reduced down to 15%.

In this section, the RS pattern of multipass T-joints at 70% penetration of S275JR plates for a thickness range from 20 to 60 mm is evaluated (see **Figure 19**). Same filler material, 1.2 mm diameter PRAXAIR M-86 filler wire, according to the AWS/ASME SFA 5.18 ER70S-6 standard, and a quasi-constant weld pass section are considered for all cases. **Table 6** shows the studied case configuration data where dimensions (wide and length) have been previously specified to avoid the influence of the edge boundary effects in the RS pattern.
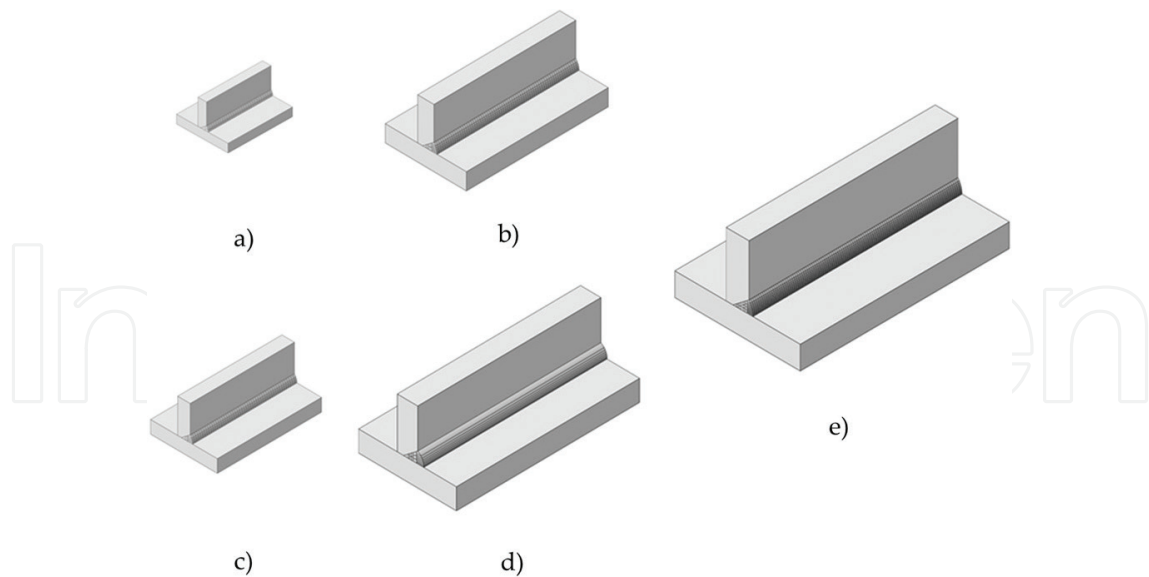
Figure 19. (a) 20 mm-, (b) 30 mm-, (c) 40 mm-, (d) 50 mm- and (e) 60 mm-thick T-joint case studies.

4.1. Numerical procedure

In this section, the modelling procedure presented in Section 2 and validated in Section 3 is used. As in Section 3, the heat transfer model as well as the mechanical model used for the simulation of the welding process of the selected case studies is implemented in the simulation software ABAQUS™.

4.2. Geometric model

In this Section, 10 mm length discretization size is used, which ensures a temporal discretization lower than 2 s in all the passes. **Figure 20** shows the numerical model of a 40-mm thick case study with 14 passes (T-joint_40).

Case study	Dimensions			Number of passes
	Thickness (mm)	Wide (mm)	Length (mm)	
T-joint_20	20	120	150	4
T-joint_30	30	160	250	8
T-joint_40	40	200	350	14
T-joint_50	50	240	450	22
T-joint_60	60	280	550	31

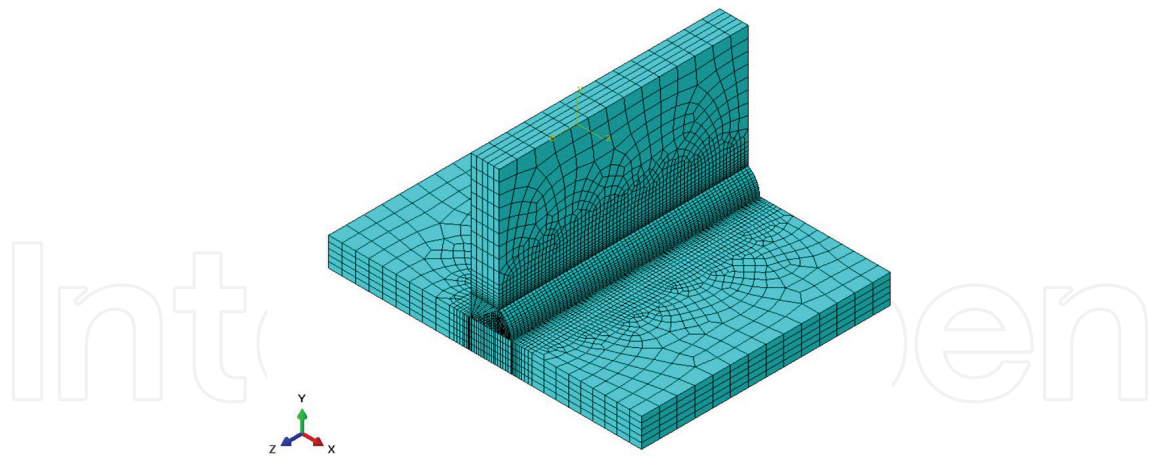**Table 6.** Case studies configuration data. Numerical procedure.

Figure 20. Numerical model of case study T-joint_40.

Case study	Pass cross section (mm^2)	Process parameters		FEM input parameters		
		Welding power (W)	Welding speed (mm/min)	Body heat flux (W/mm³)	Discret. length (mm)	Kill-rebirth rate (s^{-1})
T-joint_20	26.78	7201	388	23.37	10	0.65
T-joint_30	29.20	7310	356	21.82	10	0.59
T-joint_40	29.23	7311	356	21.82	10	0.59
T-joint_50	30.63	7471	345	21.82	10	0.58
T-joint_60	30.15	7567	345	21.93	10	0.58

Table 7. Theoretical welding process parameters and FEM input parameters.

4.3. Material

In this section, same material properties that are used in Section 3 are considered for S275JR plates and the 1.2 mm diameter PRAXAIR M-86 filler wire.

4.4. Loads and boundary conditions

The main input parameters to be implemented in the FEM model, i.e. heat source power and welding speed, have been defined according to the analytical procedure proposed in Section 2. Thus, welding speed to be implemented as element rebirth rate has been calculated for each pass by using the parabolic model constants $\alpha \approx 0.3$ mmA^{-1} s^{-1} and $\beta \approx 5 \cdot 10^{-5}$ A^{-2} s^{-1} for a 1.2 mm plain carbon steel wire as previously specified. **Table 7** shows the calculated process parameters and input parameters for the FEM model.

Finally, a natural convection boundary condition has been assumed in all surfaces exposed to air (in both plates and rebirthed weld bead elements).

4.5. Results and discussion

Figure 21 shows the RS pattern in the normal direction to the weld seam for the case of 40-mm thick T-joint as example. It can be observed that maximum stress is generated next to the weld seam.

Figure 22 shows the evolution of maximum equivalent uniaxial RS in the critical plane, which is especially interesting to conduct fatigue assessment [58], for different welded plate thickness. Two different trends clearly are observed:

- For low thickness, maximum uniaxial RS value increases from 85% of the yield stress (235 MPa) for 20 mm thickness plates up to 95% of the yield stress (261 MPa) for 40 mm thickness plates.

- In contrast, for thickness higher than 40 mm, it is observed that RS value decreases down to 66% of yield stress (182 MPa) for 60-mm thick plates.

As temperature gradients are the main responsible for RS generation, these opposite trends are attributed to the fact that when plate thickness is increased, two different phenomena occur: (i) the increase of provided total heat (directly related with the number of passes) and (ii) the increase of the heat absorption capacitance of the welded plates (directly related to the increase of the total volume).

The total supplied heat energy E_{in} can be described as de product of the heat power supplied Q_{in} and the welding time t (8):

$$E_{in} = Q_{in}t \tag{8}$$

The welding time t is dependent on the total welding length L_w and the welding speed v_s (9):

$$t = L_w/v_s \tag{9}$$

The total welding length L_w is the product of the total number of passes n and the weld pass length L_{seam} (10):

$$L_w = nL_{seam} \tag{10}$$

Thus, Eq. (8) can be rewritten as follows (11):

$$E_{in} = Q_{in}\frac{nL_{seam}}{v_s} \tag{11}$$

The number of weld passes n can be calculated based on the total cross section to weld A_w and each weld pass cross section A_s (12):
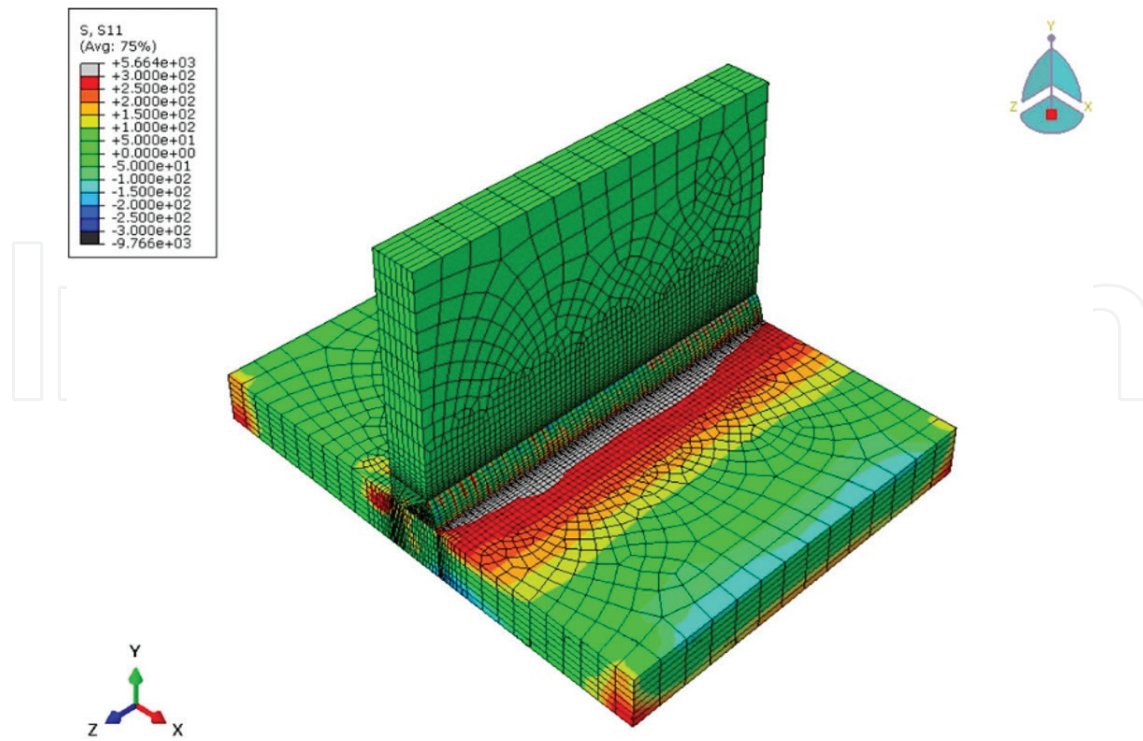
$$n = A_w/A_s \tag{12}$$

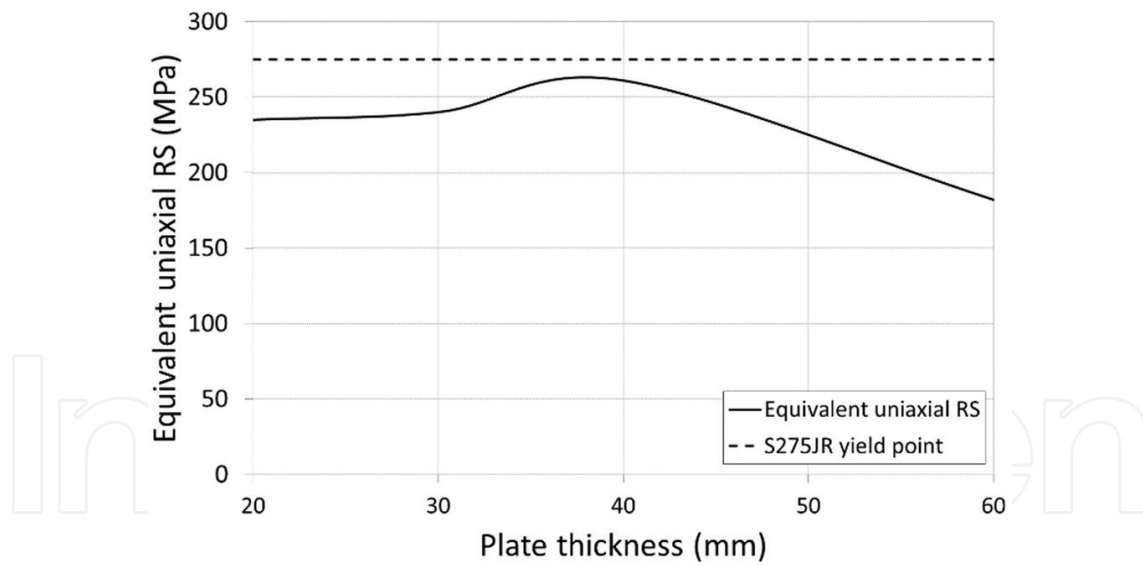**Figure 21.** RS pattern of case study T-joint_40.

Figure 22. Maximum equivalent uniaxial stress vs. thickness.

Figure 23 shows that number of passes n increases quadratic with the plate thickness th. Consequently, it can be concluded that the total heat energy supplied to the welded plates, which is proportional to the number of passes, also presents a quadratic behaviour.

On the other hand, Eq. (13) describes the heat capacitance C_{plate} of the welded plates:

$$C_{plate} = \rho \, V_{plate} \, c_p \tag{13}$$
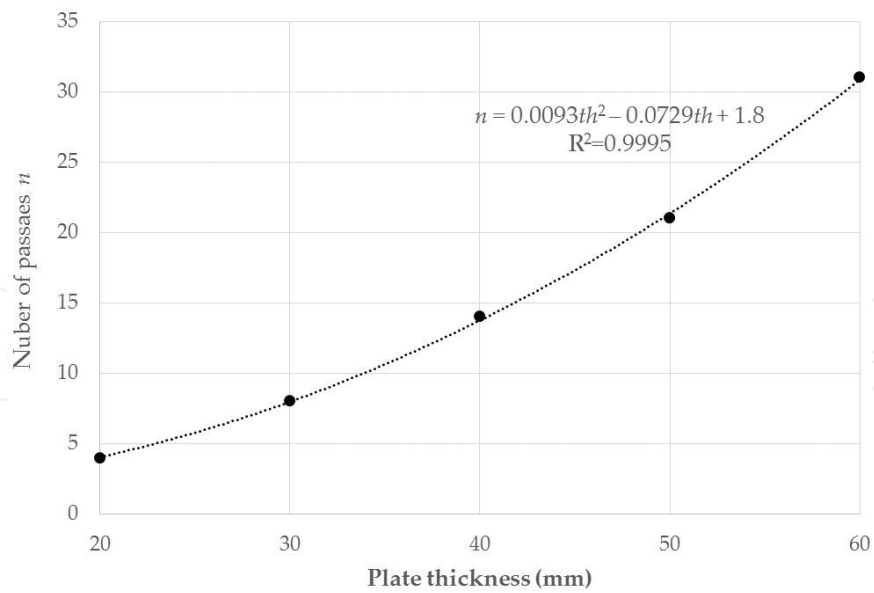
Figure 23. Number of weld passes according to plate thickness.

where ρ is the plate material density, V_{plate} is the volume of the welded plates and c_p is the specific heat of the plate material.

Figure 24 shows the evolution of the supplied total heat energy E_{in} and the heat power supply to plate heat capacitance ratio Q_{in}/C_{plate} with the plate thickness increase, which represents the plate average temperature increase rate without considering heat losses through convection. It can be observed that, even the total heat increase presents a quadratic increase, the Q_{in}/C_{plate} ratio decreases abruptly with thickness due to plate volume and, consequently, heat
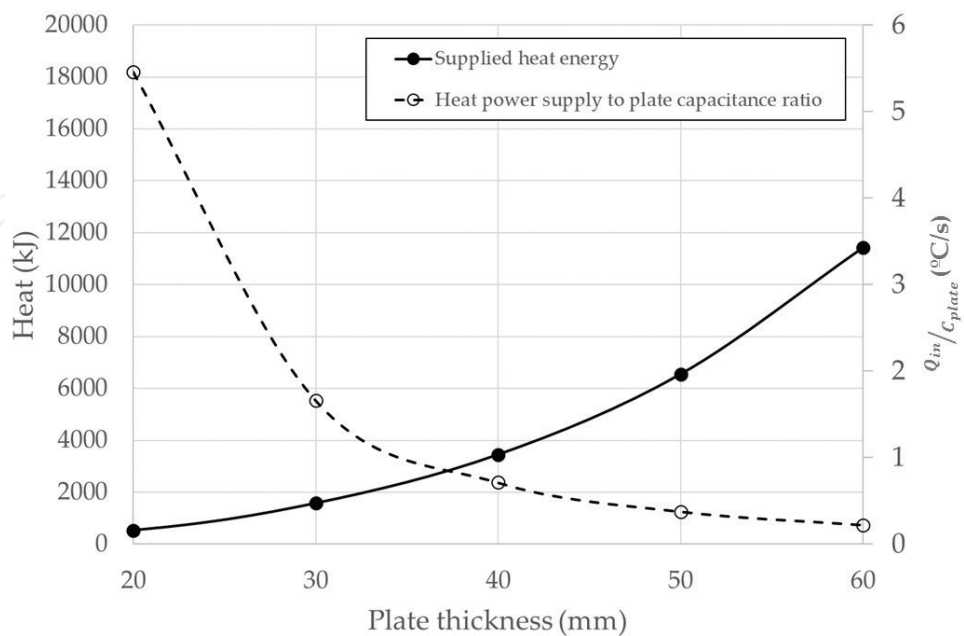
Figure 24. Evolution of total heat supply and heat power supply to plate heat capacitance ration with the plate thickness increase.

capacitance cubic increase. Thus, for plate thickness over 38 mm, the average plate temperature increase ratio is below 1°C/s. Therefore, it is observed that for low plate thickness, the provided total heat is predominant over the heat absorption capacity. In contrast, for high thickness, the heat absorption capacity increase overtakes the provided total heat effect.

5. Conclusions

In the present chapter, a procedure to predict RS pattern in spray transfer multipass welding where the heat source is defined based on the welding physics is described and validated. The procedure does not require any welding experimental characterisation to define FEM input parameters, which enables its use as a predictive tool. Results showed good correlation, with an average deviation of 9.15% in the thermal field and 42 MPa in the RS field.

Following, the influence of plate thickness and number of passes in the RS pattern of thick T-joint welds is conducted. Results have shown that, in the studied range, the assumption of considering RS value as the yield stress (YS) [18,-20] is reasonable for low thickness plates, where RS around 85–95% of YS is observed. However, RS value can decrease down to 66% of the YS for high thickness plate welds.

Author details

Jon Ander Esnaola*, Ibai Ulacia, Arkaitz Lopez-Jauregi and Done Ugarte

*Address all correspondence to: jaesnaola@mondragon.edu

Structural Mechanics and Design, Engineering Faculty, Mondragon Unibertsitatea, Mondragón, Spain

References

[1] Naidu DS, Moore KL, Ozcelik S. Modelling Sensing and Control of Gas Metal Arc Welding. Kilington: Elsevier Science Ltd.; 2003

[2] Gery D, Long H, Maropoulos P. Effects of welding speed, energy input and heat source distribution on temperature variations in butt joint welding. Journal of Materials Processing Technology. 2005;**167**(2):393-401

[3] Mousavi M, Haeri M. Estimation and control of droplet size and frequency in projected spray mode of a gas metal arc welding (GMAW) process. ISAT. 2001;**50**(3):409-418

[4] Murray PE. Selecting parameters for GMAW using dimensional analysis. Welding Journal. 2002;**81**(7):125-131

[5]   Maddox SJ. Fatigue strength of welded structures. Woodhead publishing. 1991

[6]   Sattari-FAr I, Farahani MR. Effect of the weld groove shape and pass number on residual stresses in butt welded pipes. International Journal of Pressure Vessels and Piping. 2009;**86**(11):723-731

[7]   Brickstad B, Josefson BLA. Parametric study of residual stresses in multi-pass butt welded stainless steel pipes. International Journal of Pressure Vessels and Piping. 1998;**75**(1):11-25

[8]   Keivani R, Jahazi M, Pham T, Khodabandeh AR, Afshar MR. Prediction of residual stresses and distortion during multisequence welding of large size structures using FEM. International Journal of Advanced Manufacturing Technology. 1-11

[9]   Asadi M, Goldak J, Nielsen J, Zhou J, Tchernov S, Downey D. Analysis of predicted residual stress in a weld and comparison with experimental data using regression model. International Journal of Mechanics and Materials in Design. 2009;**5**:353-364

[10] Deng D, Murakawa H. Numerical simulation of temperature field and residual stress in multi-pass welds in stainless steel pipe and comparison with experimental measurements. Computational Materials Science. 2006;**37**(3):269-277

[11] Turski M, Francis JA, Hurrell PR, Bate SK, Hiller S, Withers PJ. Effects of stop-star features on residual stresses in a multipass austenitic stainless steel weld. International Journal of Pressure Vessels and Piping. 2012;**89**:9-18

[12] Philipenko A. Computer simulation of residual stress and distortion of thick plates in multi-electrode submerged arc welding. Theri mitigation techniques. PhD thesis, Norwegian University of Science and Technology. 2001

[13] Radaj D. Heat Effects of Welding. Berlin: Springer; 1992

[14] Chang P-H, Teng T-L. Numerical and experimental investigations on the residual stresses of the butt-welded joints. Computational Materials Science. 2004;**29**:511-522

[15] Messler RW. Principles of Welding Processes, Physics, Chemistry, and Metallurgy. Troy, NY: John Wiley & Sons; 2008

[16] Paradowska A, Price JW, Ibrahim R, Finlayson T. A neutron diffraction study of residual stress due to welding. Journal of Materials Processing Technology. 2005;**164**:1099-1105

[17] Navas VG. Optimización de procesos de mecanizado mediante control de tensiones residuales y otros parámetros de integridad superficial. PhD thesis, Campus Tecnológico de la Universidad de Navarra, Spain. 2006

[18] Sonsino CM. Multiaxial fatigue assessment of welded joints-recommendations for design codes. International Journal of Fatigue. 2009;**31**(1):173-187

[19] Radaj D, Sonsino CM, Fricke W. Fatigue assessment of welded joints by local approaches. Woodhead publishing. 2006

[20]   Lassen T, Recho N. Fatigue life analysis of welded structures. London: Wiley-ISTE; 2006

[21]   Lopez-Jauregi A, Esnaola JA, Ugarte D, Torca I, Larranaga J. Procedure to predict residual stress pattern in spray transfer multipass welding. International Journal of Advanced Manufacturing Technology. 2014;**76**:2117-2129

[22]   Hansen JL. Numerical modelling of welding induced stresses. PhD thesis, Technical University of Denmark. 2003

[23]   Rosenthal D. Mathematical theory of heat distribution during welding and cutting. Welding Journal. 1941;**20**(5):220-234

[24]   Pavelic V, Tanbakuchi R, Uyehara OA, Myers PS. Experimental and computed temperature histories in gas tungsten arc welding of thin plates. Welding Journal. 1969;**48**(7):295

[25]   Goldak J, Chakravati A, Bibby M. A new finite element model for welding heat sources. Metallurgical Transactions B. 1984;**15**(2):299-305

[26]   Chen B-Q. Hashemezadeh Guedes Soares C. Numerical and experimental studies on temperature and distortion patterns in butt welded plates. International Journal of Advanced Manufacturing Technology. 2014;**72**:1121-1131

[27]   Zhu F, Xu C, Zeng L. Coupled finite element analysis of MIG welding assembly on auto-body high-strength steel panel and door hinge. International Journal of Advanced Manufacturing Technologies. 2010;**51**:551-559

[28]   Lidam RN, Manurung YHP, Haruman E. Angular distortion analysis of the multipass welding process on combined joint types using thermo-elastic-plastic FEM with experimental validation. International Journal of Advanced Manufacturing Technologies. 2013;**69**:2373-2386

[29]   Price J, Paradowska A, Joshi S, Finlayson T. Residual stresses measurements by neutron diffraction and theoretical estimation in a single weld bead. International Journal of Pressure Vessels and Piping. 2006;**83**:381-387

[30]   Barsoum Z, Barsoum I. Residual stress effects on fatigue life of welded structures using LEFM. Engineering Failure Analysis. 2009;**16**(1):449-846

[31]   Pichot F, Danis M, Lacoste E, Danis Y. Numerical definition of an equivalent GTAW heat sources. Journal of Materials Processing Technologies. 2013;**213**(7):1241-1248

[32]   Wahab MA, Painter MJ. Numerical model of gas meatal arc weld using experimentally determined weld pool shapes as the representation of the welding heat source. International Journal of Pressure Vessels and Piping. 1997;**73**(2):153-159

[33]   Barsoum Z. Residual stress prediction and relaxation in welded tubular joint. Weld World. 2007;**51**(1-2):23-30

[34]   Hu J, Tsai HL. Heat and mass transfer in gas metal arc welding. Part I: The arc. International Journal of Heat and Mass Transfer. 2007;**50**(5):833-846

[35] Hu J, Tsai HL. Heat and mass transfer in gas metal arc welding. Part II: The metal. International Journal of Heat and Mass Transfer. 2007;**50**(5):808-820

[36] Xu G, Hu J, Tsai HL. Three-dimensional modeling of ar plasma and metal transfer in gas metal arc welding. International Journal of Heat and Mass Transfer. 2009;**52**(7):1709-1724

[37] Norrish J. Advanced welding processes. Institute of. Physics. 1992

[38] Lesnewich A. Commentary on GMAW. Parameter selection paper. 2003

[39] Palani PK, Murugan N. Modeling and simulation of wire feed rate for steady current and pulsed current gas metal arc welding using 317L flux cored wire. International Journal of Advanced Manufacturing Technologies. 2007;**34**:1111-1119

[40] Murray PE. Selecting parameters for GMAW using dimensional analysis. Welding Journal. 125-131

[41] Modenesi PJ, Reis RI. A model for melting rate phenomena in GMA welding. Journal of Materials Processing Technologies. **189**:199-205

[42] Palain PK, Murugan N. Selection parameters of pulsed current gas metal ar welding. Journal of Materials Processing Technologies. 2006;**172**:1-10

[43] Zamiri-Akhlaghi F. Welding simulation and fatigue assessment of tubular K-joint in high-strength steel. PhD thesis, École Polytechnique Fédérale de Lausanne, Switzerland. 2014

[44] Teng TL, Fung CP, Chang PH. Effect of weld geometry and residual stresses on fatigue in butt-welded joints. International Journal of Pressure Vessels and Piping. 2002;**79**:476-492

[45] Payares-Asprino MC, Katsumoto H, Liu S. Effect of martensite start and finish temperatures on residual stress development in structural steel welds. Welding Journal. 2008;**87**:279-289

[46] Deng D. FEM prediction of welding residual stress and distortion in carbon steel considering phase transformation effects. Materials and Design. **30**(2):359-366

[47] APTA (Asocación para la Promoción Técnica del Acero) [Internet]. Available from: http://apta.com.es/pdf/aceros.pdf [Accessed: 11-06-2014]

[48] Electric L. GMAW welding guide [Internet]. Available from: hhtp://www.oemeyer.com/Media/Defautl/Industrial/technical/MIG%20welding%20guide-lincoln.pdf [Accessed: 11-06-2014]

[49] Ranjabamodeh E, Pouranavari M, Fischer A. Influence of welding parameters on residual stresses in dissimilar HSLA steels welds. Association of Metallurgical Engineers of Serbia. 2013

[50] Mills KC. Recommended Values of Thermophysical Properties for Selected Commercial Alloys. Cambridge, England: Woodhead Publishing; 2002

[51] Thermal conductivity for carbon steel AISI 1010 [Internet]. Available from: http://www.egunda.com/materials/alloys/carbon_steels/show_carbon.cfm?ID=AISI_1010&show_prop=tc&Page_Title=Carbon%20Steel%20AISI%201010 [Accessed: 11-06-2014]

[52] Pitz M. Merklein M. FE simulation laser assisted bending. Proceedings of the 11th International Conference: Sheet Metal. 745-752

[53] Tensile properties at high temperature for S275 steel [Internet]. Available from: http://www.thyssenfrance.com/fich_tech_en.asp?product_id=17930 [Accessed: 11-06-2014]

[54] EN 1993-1-2: Eurocode 3: Design of Steel Structures-Part 1-2: General Rules-Structural Fire Design. 2005

[55] Safety data sheet for Stargon 82 [Internet]. Available from: http://www.cialgas.com/wp-content/uplads/2012/09/STARGON-82.pdf [Accessed: 11-06-2014]

[56] Larrañaga J. Geometrical accuracy improvement in flexible roll forming process by means of local heating. PhD thesis, Mondragon Unibertsitatea. 2011

[57] Withers PJ, Bhadeshia HKDH. Residual stress. Part 1-measurement techniques. Materials Science and Technology. 2001;**17**(4):355-365

[58] Lopez-Jauregi A, Esnaola JA, Ulacia I, Urrutibeaskoa I, Madariaga A. Fatigue analysis of multipass welded joints considering residual stresses. International Journal of Fatigue. 2015;**79**:75-85